



Corrosion of stainless steel and molybdenum used as PCC in Na//Sb-Bi liquid metal batteries under cycling conditions

Renate Fetzler^{*}, Tianru Zhang, Annette Heinzl, Alfons Weisenburger, Georg Müller

Institute for Pulsed Power and Microwave Technology (IHM), Karlsruhe Institute of Technology (KIT), Hermann-von-Helmholtz-Platz 1, 76344, Eggenstein-Leopoldshafen, Germany

HIGHLIGHTS

- 316-type steel forms solid Sb-compounds in static SbBi_9 and in operating LMB cell.
- Corrosion of stainless steel is slightly enhanced under cycling conditions.
- The steel is protected by thin oxide layer when statically exposed to Na-Sb-Bi.
- Mo shows very good corrosion resistance both in static and in cycling conditions.

ARTICLE INFO

Keywords:

Corrosion
Austenitic steel
Molybdenum
Positive current collector (PCC)
Liquid metal battery (LMB)
Liquid sodium
Liquid Sb-Bi alloy

ABSTRACT

Material compatibility is a major challenge in the development of liquid metal batteries. In this study, the corrosion behavior of two candidate positive current collector materials, austenitic stainless steel and molybdenum, in Na//SbBi₉ liquid metal batteries is investigated. In-situ corrosion in operating cells is compared with static corrosion in SbBi₉ (corresponding to the fully charged state) and Na_{0.30}Sb_{0.07}Bi_{0.63} (representing the fully discharged state) at 450 °C. Stainless steel shows a much better corrosion resistance in Na-Sb-Bi alloy (corrosion depth below 1 μm after 750 h static exposure) than in SbBi₉ (7–9 μm corrosion layer) thanks to the formation of a thin oxide layer. The corrosion under cycling conditions shows similar characteristics (formation of solid Fe-Cr-Ni-Sb compounds), though accelerated, as static exposure to SbBi₉. Molybdenum exhibits a very good corrosion resistance both in static and in cycling conditions, showing merely a minor dissolution into the adjacent alloy.

1. Introduction

Liquid metal batteries (LMB) are an emerging technology for grid-scale stationary energy storage [1–4]. Due to the liquid nature of the electrodes and the electrolyte, rapid kinetics is achieved at the electrode/electrolyte interfaces and the LMB cells do not suffer from structural degradation upon cycling. Furthermore, good scalability, easy temperature management, and low costs offer attractive options for large scale devices. However, due to the elevated working temperature, corrosion issues are enhanced and may substantially limit the service lifetime of LMB cells. Therefore, the material compatibility of each specific cell type and, in particular, corrosion of the positive current collector (PCC) in contact with the liquid positive electrode, need thorough investigation.

Corrosion of structural or PCC materials exposed to liquid metals is driven by the mutual solubility of the alloying elements and by the

formation of intermetallic compounds and solid solutions at the interface between solid material and liquid metal. Steel alloying elements Fe, Cr, and Ni, for instance, have considerable solubility in liquid metals such as lead, tin, or bismuth [5]. Especially at high temperature, the high solubility results in severe dissolution corrosion [6,7]. Differences in the solubility of different steel alloying elements lead to selective dissolution, facilitating penetration of liquid metal into the steel. Some liquid metals (e.g., antimony or tin) form solid intermetallic compounds with steel alloying elements. If such compounds and other solid corrosion products build a compact layer on the steel surface, they can mitigate diffusion and material exchange and thus slow down dissolution corrosion considerably. However, when solid compounds form detached from the surface, they can enable continuous dissolution even beyond the solubility limit [7]. In contrast to static exposure conditions, a positive current collector in an operating LMB cell is exposed to the liquid

^{*} Corresponding author.

E-mail address: renate.fetzer@kit.edu (R. Fetzler).

<https://doi.org/10.1016/j.jpowsour.2024.235473>

Received 5 August 2024; Received in revised form 3 September 2024; Accepted 15 September 2024

Available online 18 September 2024

0378-7753/© 2024 The Authors. Published by Elsevier B.V. This is an open access article under the CC BY-NC license (<http://creativecommons.org/licenses/by-nc/4.0/>).

positive electrode under cycling conditions. During cycling, the concentration of the negative electrode metal in the positive electrode continuously varies. In addition to the dynamically changing chemistry, electric currents, potential differences, and fluid flow may influence the corrosion process.

In recent years, LMBs based on lithium (Li) as negative electrode were widely researched [8–11]. Li provides high energy density, low melting temperature, and low solubility in Li halide salts. Therefore, it does not surprise that also corrosion studies on PCC materials in cycling conditions are reported for Li-based LMBs only. A study on Li//Sb-Pb LMB cells [12] showed that corrosion layers composed of Fe-Sb and Fe-Cr-Ni-Sb compounds that formed on low-carbon steel and stainless steel (SS) 301, respectively, during static exposure to Sb-Pb were destroyed when the steels were employed as PCC under cell operating conditions. The Fe-Cr-Sb corrosion layer formed on SS 430 was stable even in cycling conditions. The destruction of the corrosion layers was attributed to the variation in Li concentration of the positive electrode during cycling and the preferential alloying of Li with Sb. Similarly, a study on corrosion of SS 304 in Li//Sb-Sn LMBs found no Fe-Sb corrosion products in cycling conditions and after static exposure to Li-Sb-Sn alloy, corresponding to the fully discharged state, although static exposure to Sb-Sn alloy resulted in formation of an Fe-Sb layer on the surface of SS 304 [13]. It was reasoned that alloying of the positive electrode with Li leads to destruction of the Fe-Sb compounds and to formation of a solid Li-Sb alloy due to the preferential reaction of Li with Sb, leaving behind liquid Sn that directly contacts the steel and causes enhanced corrosion. Finally, cycling conditions in Li//Sb-Bi-Sn cells at 500 °C led to destruction of the solid Fe-Sb and Fe-Cr-Sb compounds that formed and protected the steel when 304 was statically exposed to Sb-Bi-Sn alloys [14]. Upon discharging, Li reacted first with Sb and formed solid Li_3Sb , followed by the reaction with Bi and formation of solid Li_3Bi . As in the Li//Sb-Sn system, the lithiation process leaves behind liquid Sn, a strongly corrosive liquid metal in contact with steels. Common to all these studies, the reported effects of cycling conditions on corrosion are related with and attributed to a dynamically changing composition of the positive electrode. To the best of our knowledge, there is only one study that reports other effects of cell cycling on corrosion: The authors of Ref. [15] investigated the applicability of titanium, molybdenum, and tungsten as PCC material in Li//Sb-Sn cells. In case of W, cycling conditions were supposed to increase flow-induced erosion and cavitation corrosion. Mo showed considerable dissolution in Sb-Sn already in static conditions (about 8 μm in 1000 h).

As an alternative option to Li-based LMBs, sodium (Na) was researched in recent years as negative electrode metal because of its high abundance and related economic and environmental advantages over Li. The major concern of Na used as negative electrode in an LMB is its high solubility in Na halide salts. This issue could be mitigated recently by using the multi-cationic salt mixture LiCl-NaCl-KCl as electrolyte. With a low amount of NaCl (around 5 mol%) added to eutectic LiCl-KCl (59.2–40.8 mol%), both the melting point and the Na solubility of the electrolyte could be reduced to reasonable values while keeping a sufficiently high Na^+ ion conductivity [16,17]. Combined with the antimony-bismuth alloy SbBi_9 as positive electrode, Na-based LMB test cells demonstrated very promising electrochemical performance [17, 18]. The Sb-Bi alloy was selected because of its lower corrosivity towards potential PCC materials compared with Sb-Sn alloys [19–22]. This concerns not only Fe-based materials but also Mo. Despite the lower corrosivity of SbBi_9 , when stainless steel was used as positive current collector (PCC), the cell performance declined significantly after 800 h of operation [18]. Preliminary investigation of the cell components after cell operation showed that the stainless-steel PCC suffered from corrosion where it had been in direct contact with the positive electrode during operation.

The aim of the present study is to investigate corrosion of PCC materials in a Na//Sb-Bi LMB under cycling conditions and to evaluate whether the corrosion observed after operation is caused solely by the

composition variations of the positive electrode during cycling. In contrast to the previous studies on Li-based cells, the amount of Na used in the present Na-based LMBs is lower relative to the total amount of positive electrode. This means that the positive electrode remains liquid during the entire discharge process; there is no separation of solid and liquid phase, the latter being more aggressive towards PCC materials than the positive electrode alloy in fully charged state.

To shed light on the influence of cycling conditions of Na-based LMBs on the corrosion of PCC materials, the present study employs LMB test cells with the active components Na/LiCl-NaCl-KCl/ SbBi_9 . Corrosion experiments representing three different situations are compared. (1) Static corrosion of PCC materials exposed to the positive electrode alloy SbBi_9 not containing any Na. This corresponds to the fully charged state of the respective LMB cell. (2) Static corrosion tests in Na-Sb-Bi alloy with 30 mol% Na added to SbBi_9 , corresponding to the fully discharged state of the present LMB with 0.2 mol Na, 0.065 mol Sb, and 0.585 mol Bi. (3) Corrosion of the PCC in a fully operational LMB test cell under cycling conditions. These three situations are compared for two different classes of PCC materials, stainless steel and molybdenum. Stainless steels are the most commonly used structural materials. They show moderate corrosion rates both in static exposures to SbBi_9 [22] and in preliminary investigations of the material after its service as PCC in an operating cell [18]. The second material selected for this study, molybdenum, has high static corrosion resistance to SbBi_9 [22] and is therefore a very promising material to be used as PCC in Na// SbBi_9 cells.

2. Materials and methods

2.1. Materials

The candidate PCC materials tested in this work were three different austenitic stainless steels (304, 316L, 316Ti) and molybdenum (Mo) metal. The stainless steels were obtained from the KIT inventory. Respective compositions are listed in Table 1. The Mo sheets (purity >99.97 %) for the static exposure tests were obtained from Plansee SE. The custom-made Mo crucible (purity >99.95 %) employed as PCC in the operating cell was delivered by BeamTec GmbH.

Antimony (purity 99.99 %, granular size 1–6 mm) and bismuth (purity 99.99 %, granular size <5 mm) were obtained from HMW Hauner GmbH & Co. KG. Sodium (purity 99.8 %) was delivered by Haines & Maassen Metallhandelsgesellschaft GmbH as blocks.

2.2. Static corrosion tests

All specimens used for the static corrosion tests were cut to appropriate size, ground by sandpaper down to a grit size of 1200, and cleaned with ethanol prior to exposure.

For preparation of the Sb-Bi alloy, Sb granules and Bi granules were mixed in alumina crucibles in a molar ratio of 1:9. Melting and pre-conditioning (removal of remaining oxides) of the SbBi_9 alloys as well as the static exposure tests in molten SbBi_9 took place in the COSTA facility, which consists of a quartz glass tube inside a tubular furnace and a gas control system [7]. The alumina crucibles containing Sb and Bi granules were placed inside the glass tube. Then, the glass tube was purged with 100 mL/min flow of an Ar- H_2 gas mixture (argon, purity 6.0, mixed with 5 % hydrogen, purity 6.0) and the temperature was held at 700 °C until complete melting and removal of excess oxygen from the Sb-Bi alloy was obtained. Finally, the temperature was reduced to the

Table 1
Composition of tested stainless steels as measured by SEM-EDS (in wt. %).

Material	Si	Mn	Cr	Mo	Ni	Ti	Fe
304	0.8	1.7	18.6	–	7.6	–	Bal.
316L	1.2	1.6	15.1	3.1	14.8	–	Bal.
316Ti	0.7	1.1	17.3	3.3	9.8	0.3	Bal.

test temperature of 450 °C and a glovebox with oxygen-poor atmosphere was connected to the glass tube for loading the test specimens. Each crucible contained only one specimen. Specimens from stainless steel 316L and from molybdenum were tested, see Table 2. The ratio of exposed sample surface to liquid metal volume was below 300 cm²/L. The oxygen partial pressure in the gas atmosphere was between 10⁻³⁶ and 10⁻³⁴ bar during the entire exposure test, which corresponds to an oxygen potential $RT \ln(p_{O_2})$ between -500 and -470 kJ/mol O₂. After the test duration of 740 h, the specimens were extracted and cooled down to room temperature under controlled atmosphere in the glovebox. For further details on the static exposure experiments to liquid SbBi₉, we refer to our previous publication [22].

For preparation of the Na-Sb-Bi alloy, first SbBi₉ alloy (120 g) was prepared in an alumina crucible and preconditioned in the COSTA facility as described above. After cooling down under controlled atmosphere, the alumina crucible with the preconditioned SbBi₉ alloy was transferred to a glovebox (Ar atmosphere with O₂ < 1 ppm, H₂O < 0.5 ppm) for further steps. Inside the glovebox, liquid Na was purified in a specially designed sodium sink. The preconditioned SbBi₉ alloy was melted and poured into a heated stainless-steel crucible. Then, 4.1 g of liquid Na from the purification sink was added to obtain Na-Sb-Bi alloy with 30 mol% Na, i.e., Na_{0.30}Sb_{0.07}Bi_{0.63}. The readily prepared Na-Sb-Bi alloy was evenly distributed into six Mo crucibles and each crucible was loaded with one specimen to be tested. Specimens from all materials were used for these exposure tests, see Table 2. The exposed sample surface to liquid metal volume ratio was around 800 cm²/L. After cooling down to room temperature, the Mo crucibles were set inside tailor-made stainless-steel containers, Zr foil was added as sealing, and the containers were closed and hermetically sealed, see Fig. 1a. Finally, the sealed containers were transported to a special COSTA facility equipped with a stainless-steel tube inside the tubular furnace. During the exposure test, the containers remained sealed and the gas atmosphere inside the tube was controlled by a continuous flow of Ar-5%H₂ gas. The static exposure experiment in Na-Sb-Bi alloy was performed at 450 °C for 750 h. The described procedure using sealed containers is required to avoid evaporation of Na and because the enthalpy of formation of the Na oxide Na₂O (-640 kJ/mol O₂) is below the oxygen potential achieved by the Ar-5%H₂ gas mixture. Continuous exposure to such an atmosphere would thus result in continuous oxidation of Na.

2.3. Corrosion tests under cycling conditions

Cycling conditions were provided by a fully operational Na-based LMB cell with SbBi₉ alloy serving as positive electrode. Details on the preparation and electrochemical performance of the cells can be found in Ref. [18]. Fig. 1b shows the design of the cell, in which the cell body served as positive current collector. It was made of stainless steel 316Ti, the material to be tested under cycling conditions. Assembly of the test cell took place in the glovebox (Ar atmosphere with O₂ < 1 ppm, H₂O < 0.5 ppm). The cell body was filled with 130 g of SbBi₉ alloy, which was prepared and preconditioned beforehand in the COSTA facility as described above. The ratio of exposed PCC material to positive electrode volume was around 2700 cm²/L.

The negative electrode, about 5 g of liquid Na, was hosted by a Ni foam. Sodium from the purification sink was poured into a glass container and the Ni foam was submerged. Vacuum conditions were used to force the liquid Na into the pores of the Ni foam. After cooling

Table 2
Summary of exposure tests and test conditions.

Material	static test in Sb-Bi	static test in Na-Sb-Bi	in-situ test in cycling cell
304	-	750 h @ 450 °C	-
316L	740 h @ 450 °C	750 h @ 450 °C	-
316Ti	-	750 h @ 450 °C	1500 h @ 435 °C
Mo	740 h @ 450 °C	750 h @ 450 °C	1200 h @ 435 °C

down, the foam with the solidified Na was fixed to a foam holder with Mo wires and screwed to the negative current collector, which was connected via a feedthrough with the cell cover (Fig. 1b).

The salt mixture LiCl-NaCl-KCl (61-3-36 mol%) was prepared in a stainless-steel container and dehydrated at 150 °C and 300 °C, successively, for 30 min each. Then, the salt was melted at 600 °C and poured into the cell body that already contained the positive electrode. Finally, the cell cover (including feedthrough, negative current collector, and negative electrode) was added and the cell was hermetically closed.

For testing the corrosion behavior of Mo under cycling conditions, a cell was assembled with an additional Mo crucible placed inside the cell body. The SbBi₉ alloy was poured into the Mo crucible, which served as positive current collector. All other assembly steps were adapted from the previously described cell design.

For cell operation, the test cells were put in heating sleeves and heated from below to the specified operation temperature. Due to an existing temperature gradient inside the cells, the set temperature of 500 °C corresponded to a positive electrode temperature of ~435 °C, an electrolyte temperature of ~430 °C, and a vapor temperature close to the cell cover of ~350 °C. These values resulted from measurements using a cell with implemented thermocouples.

The cell with stainless steel 316Ti as PCC material was at working temperature for 1500 h in total, thereof 1336 h under continuous charge-discharge cycling with constant-current constant-voltage (CCCV) charging and CC discharging. The cell was charged with 2.83 A (corresponding to 100 mA/cm² related to the interface between positive electrode and electrolyte) to a terminal voltage of 0.98 V. Then, at this voltage limit, the cell was further charged until the current dropped below 1.0 A. After a short relaxation step without current, the cell was discharged at a constant current of -2.83 A to the lower voltage limit of 0.5 V. Typical cycles are shown in Fig. 1c. From the open circuit voltages after charging and discharging, it is deduced that the Na content of the positive electrode varied between 5 and 22 mol% during operation. After 550 cycles, the operation of the cell was stopped deliberately (the cell was still fully functional). During disassembly, the molten salt electrolyte and the liquid positive electrode were poured out of the cell body. After cooling down under controlled atmosphere, the cell body was cut without further cleaning in appropriate pieces for analysis.

The cell containing Mo as PCC material was operated for 1200 h in total. After some other tests with different currents, the continuous cycling test (CC charging and CC discharging) started about 300 h after the cell was heated to its operation temperature. The cell was charged/discharged with ± 4.93 A (corresponding to 200 mA/cm², note the reduced surface of the positive electrode due to the introduction of the Mo crucible into the cell) to the voltage limits 1.2 and 0.45 V, see Fig. 1d for typical cycles. There was no particular reason for using different charging methods for the different cells. The positive electrode of the cell with Mo PCC contained 6–20 mol% Na during cycling, as determined from the open circuit voltages after charging/discharging. The charge-discharge cycling test was stopped after 680 cycles and around 900 h, which sums up to a total operation time of 1200 h.

2.4. Post-exposure analysis

The specimens from all corrosion tests were cut in appropriate pieces without removal of adherent Sb-Bi or Na-Sb-Bi alloy. Then, all pieces were cold-mounted in resin, ground, and polished down to 1 μm diamonds for cross-section analysis. Due to shrinkage of the resin during curing at normal pressure, a small gap appears in some locations between sample and attached alloy. Scanning electron microscopy (SEM, Zeiss LEO 1530 VP, accelerating voltage 20 kV) with an energy dispersive X-ray spectrometer (EDS) was used for examination of the cross-sections.

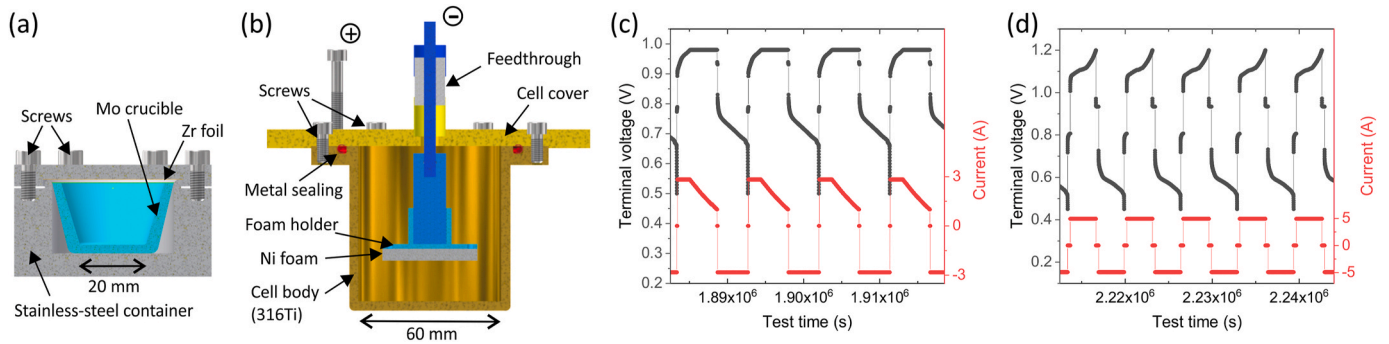


Fig. 1. (a) Design of sealed container for static exposure tests to Na-Sb-Bi alloy. (b) Design of LMB cell used for in-situ corrosion tests. (c, d) Typical charge-discharge cycles of the cells during the in-situ corrosion tests of 316Ti (c) and Mo (d).

3. Results

3.1. Static corrosion in Na-Sb-Bi alloy

All three austenitic stainless steels show a very mild corrosion attack after 750 h static exposure to Na-Sb-Bi alloy at 450 °C, see Fig. 2. Note that the low Sb content (around 3–5 at%) of the Na-Sb-Bi alloy is caused by decomposition of the alloy upon cooling to room temperature. As shown in Fig. 3b, large (10–20 μm), kidney-shaped regions enriched in Sb (~20 at%) were found embedded in the Sb-poor matrix that is visible in Fig. 2. The low Na content (around 5–8 at%) of the Na-Sb-Bi alloy is explained by the contact of the cross-section samples with water during their preparation. If not prevented by a strong chemical bond, Na reacts with the water and is washed away.

Common to all steels, the following observations are made.

- (1) Bi penetrates into the sample. The concentration of Bi smoothly decays over a distance of 0.5–1 μm into the sample, indicating a diffusive process. In some locations, this smooth decay is superimposed by a local accumulation of Bi in a subsurface layer (shoulder in EDS concentration profile), also visible as bright contrast in the SEM-BSE (backscattered electrons) image, see label “Cor” in Fig. 2a. Very similar observations are made for Sb and Na, though less visible in the EDS data due to their generally lower concentration. Nevertheless, also Sb and Na penetrate into

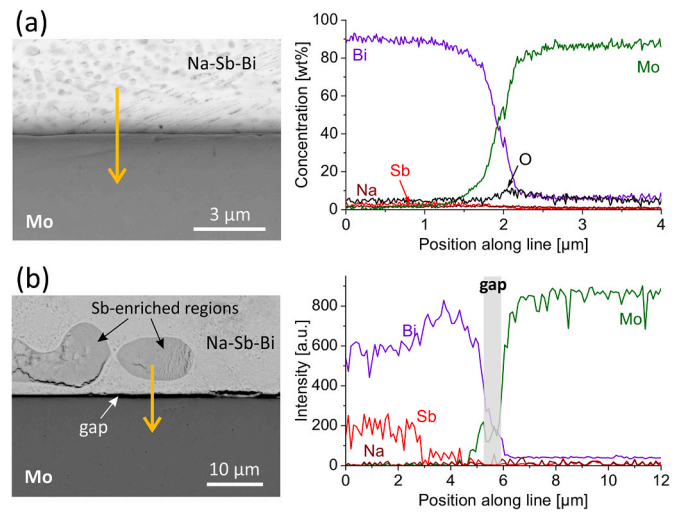


Fig. 3. SEM-BSE cross-section images of Mo after static exposure to liquid Na-Sb-Bi alloy, together with EDS elemental composition along specified lines. (a) Location with adherent alloy, (b) location with small gap between Mo and alloy (O signal not shown) and with Sb-enriched regions formed during cooling.

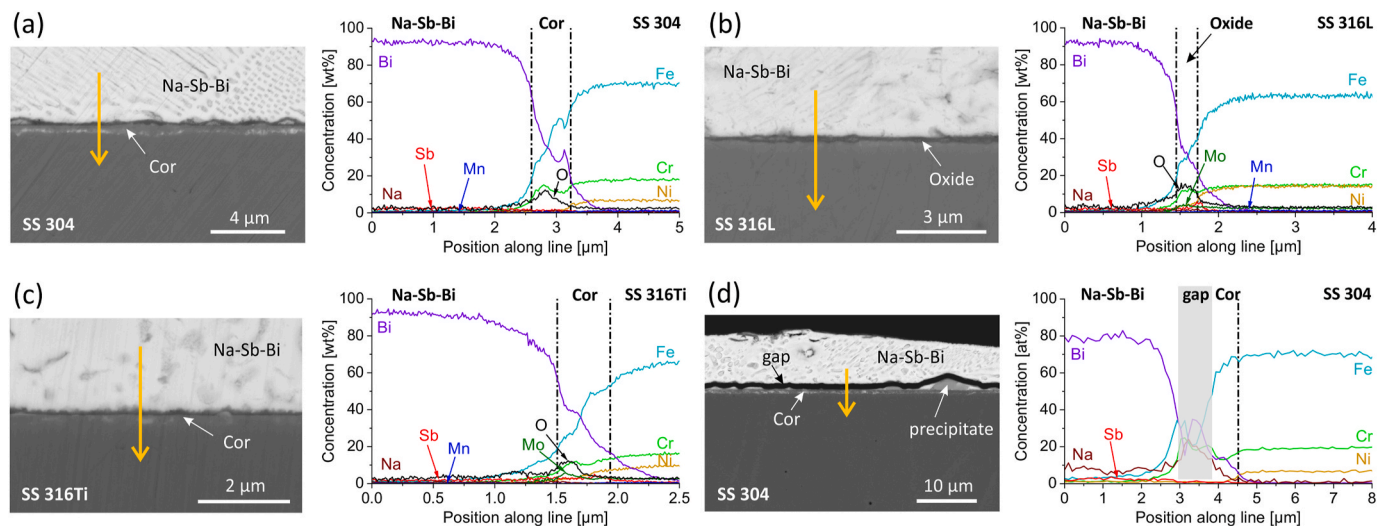


Fig. 2. SEM-BSE cross-section images of the stainless steels 304 (a), 316L (b), and 316Ti (c) after static exposure to liquid Na-Sb-Bi alloy, together with EDS elemental composition along specified lines (in wt%). Corroded regions are labelled “Cor”, oxide scale formation is marked with “Oxide”. (d) EDS elemental line scan at location with gap between specimen and Na-Sb-Bi alloy (concentration given in at%; data of O, Mn, and Mo are not shown). Data in the gap are meaningless and therefore masked in grey.

the steels. In some locations, the concentration profile of Sb shows a shoulder in a subsurface layer in some locations, see Fig. 2c, while the penetration of Na becomes visible when the data are presented in at%, see Fig. 2d. The data of Fig. 2d also confirm that the penetration of Na-Sb-Bi alloy components into the steels (and the outward diffusion of Fe and Cr, see observation (2)) is not an apparent effect caused by the limited lateral resolution of EDS analysis (finite interaction volume).

- (2) The main steel alloying elements Fe, Cr, and Ni are dissolved into the adjacent Na-Sb-Bi alloy. Both Fe and Cr show a significant content in the adjacent Na-Sb-Bi alloy next to the sample surfaces (see Fig. 2d in particular), which smoothly decays over a distance of around 0.5 μm . Ni is found homogeneously distributed in Na-Sb-Bi alloy. On the sample side, all three main alloying elements show a smooth decay towards to sample surface, complementary to the increasing Bi content. In addition to the smooth decay, Cr and Ni are depleted close to the sample surface. Finally, Cr shows a local enrichment at the sample surface, which coincides with a local oxygen enrichment.
- (3) A clear enrichment of oxygen is found at the sample surface (dark contrast in BSE images, peak of oxygen signal in EDS concentration profiles), which indicates formation of an oxide layer. The thickness of this oxide layer ranges from below 100 nm to around 400 nm. The oxygen enrichment coincides with the local enrichment in Cr, which suggests formation of a Cr-rich oxide.
- (4) The minor steel alloying elements Mn (all stainless steels) and Mo (316L and 316Ti) show deviating behavior. While Mn is found homogeneously dissolved in the Na-Sb-Bi alloy and depleted in the corroded surface layer, Mo is not found in the Na-Sb-Bi alloy but is, in some locations, slightly enriched at the sample surface.

The described results apply to all three stainless steels tested. Hereby, the variation of the corrosion layer characteristics and thickness within each sample is larger than the variation between the different steels.

Fig. 3 shows the Mo specimen after static exposure to Na-Sb-Bi alloy at 450 $^{\circ}\text{C}$. Apparently, a small, slightly asymmetric interdiffusion of Bi and Mo is observed at the interface, see Fig. 3a, suggesting that the dissolution of Mo into the adjacent alloy is more pronounced than the diffusion of Bi into Mo. To confirm that the diffusion-like concentration profiles are not caused by the limited spatial resolution of SEM/EDS analysis only, Fig. 3b shows the elemental signals across a gap between the Mo specimen and the adjacent Na-Sb-Bi alloy in units of signal intensity. Mo is clearly found in the Na-Sb-Bi alloy, confirming a minor dissolution of Mo and its diffusion into the liquid metal. No other signs of corrosion are detected along the entire surface of the Mo specimen, in particular no oxide formation. The small oxygen signal in the Mo (Fig. 3a) most probably stems from oxidation of the cross-section sample after preparation.

3.2. Static corrosion in Sb-Bi alloys

The results of the static corrosion tests of SS 316L and Mo in liquid SbBi₉ alloy at 450 $^{\circ}\text{C}$ are published in Ref. [22]. Due to their relevance for the present study, the main results are summarized here. It should be

noted that Sb with lower purity (99.65 %) was used in the previous study. As a consequence, the SbBi₉ alloy contained a small impurity from arsenic, which accumulated in some locations in large concentration and formed As-rich corrosion products on the specimen surfaces.

Fig. 4a shows a typical cross-section image of SS 316L after 740 h static exposure to SbBi₉ at 450 $^{\circ}\text{C}$. No oxide layer is found on the sample surface. Instead, a corrosion layer (light grey) of around 7–9 μm thickness is observed, which contains ~45 at% Sb, ~40 at% Fe, ~9 at% Cr, and low amounts of Ni and Bi (~3 at% each). It is supposed that this layer is mainly composed of the stable intermediate compounds FeSb and CrSb (both are non-stoichiometric compounds), which form a solid solution (Fe,Cr)Sb. The solid solution might also contain a minor contribution from the non-stoichiometric compound NiSb. Directly at the specimen surface, an additional up to 4 μm thick dark grey layer appears, which contains ~35 at% As, ~40 at% Fe, and ~25 at% Cr. The specimen surface is decorated with As-rich precipitates (~53 at% As, ~35 at% Fe, ~10 at% Cr). Since both the dark grey layer and the precipitates on the sample surface consist of As-rich compounds, they will not form in As-free SbBi₉ alloy. It can be further assumed that the light grey homogeneous corrosion layer forms irrespective of the presence or absence of As. Since its thickness does not noticeably deviate from the 7–9 μm even in locations without the As-rich dark layer on top, it is concluded that the As impurity has no significant influence on the growth rate of the Fe-Cr-Sb corrosion layer during static exposure to liquid SbBi₉ alloy.

Mo shows good corrosion resistance to liquid SbBi₉ in the static corrosion tests, see Fig. 4b. After 740 h at 450 $^{\circ}\text{C}$, a small accumulation of the As impurity is found at the interface between Mo and Sb-Bi alloy. Additionally, some diffusion of Mo into the Sb-Bi alloy is observed. It remains unclear whether the diffusion is influenced by the presence of As at the interface. As in case of the stainless steel, no oxidation of the sample surface is observed after static exposure to SbBi₉.

3.3. Corrosion under cycling conditions

Figs. 5 and 6 show the corrosion attack of the PCC material 316Ti at various locations at the bottom of the cell after 1500 h at operating temperature (1336 h continuous cycling). Although the observed corrosion layers look different on a first glance, common features and similar compositions of the various regions are identified. Common to all, both Cr and Ni show a sharp decline in concentration at the corrosion front, i.e., at the interface between the pristine material and region A (Fig. 5). The Fe content, on the other hand, transitions more (b, c) or less (a) smoothly in region A from its bulk value to the much lower value found in region B. This decrease in Fe concentration is accompanied by an increase of the Sb content and the presence of low amounts of Bi. The laterally deviating thickness of region A in Fig. 5a is directly related with a locally varying Cr content of the 316Ti base material as visualized in the corresponding elemental mapping images shown in Fig. 6a. Note that the inhomogeneous composition of 316Ti observed in Fig. 6a (Cr-rich, Ni-depleted regions: δ -ferrites) and Fig. 6b (Ti-rich precipitates: TiN and TiC) is caused during the manufacturing process; the distribution of these features is random. The Ti-rich precipitates do not seem to have any influence on the corrosion behavior.

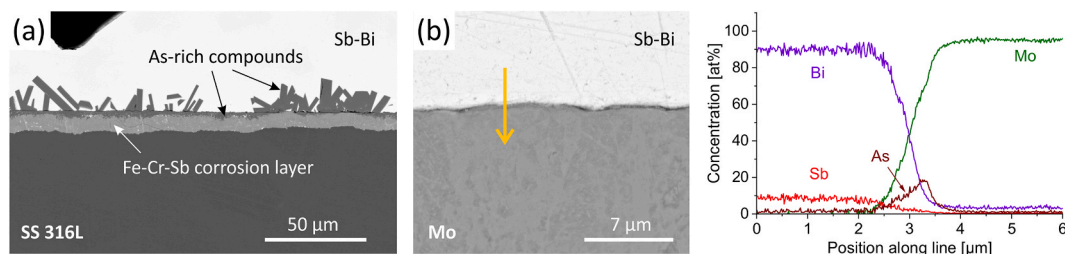


Fig. 4. SEM cross-section analysis of SS 316L (a) and Mo (b) after 740 h static exposure at 450 $^{\circ}\text{C}$ to SbBi₉ alloy with a small As impurity. Data published in Ref. [22].

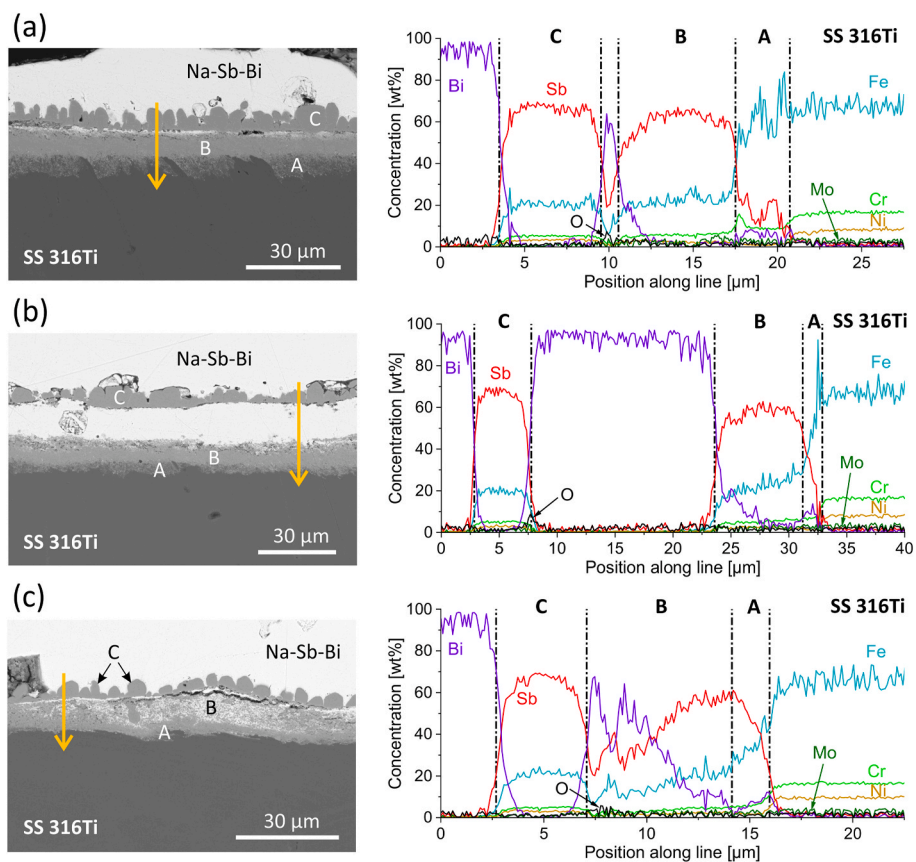


Fig. 5. SEM cross-section analysis (SEM-BSE image and EDS elemental composition along selected line) of corrosion layer of SS 316Ti after 1500 h service as PCC in an operating cell. (a) and (b) at central part of cell, (c) next to cell edge. Signals from Na, K, Cl, and Ti are very low everywhere along the lines and are, therefore, not shown for better clarity.

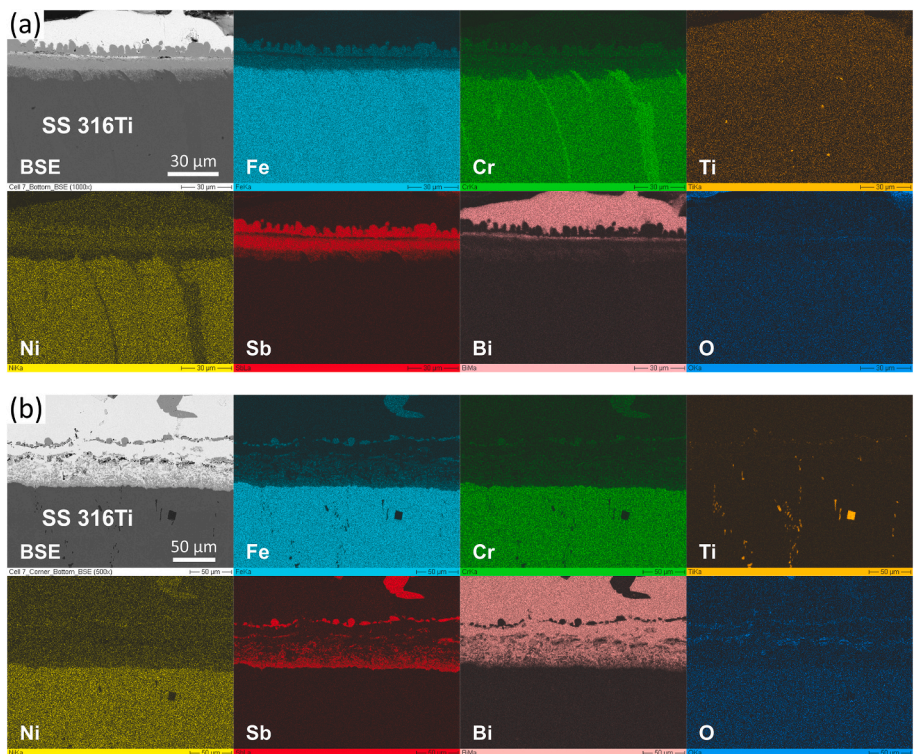


Fig. 6. SEM-EDS elemental mapping of SS 316Ti after exposure to cycling conditions in a Na//SbBi₃ LMB cell at the cell center (a) and at the cell edge (b).

In region B (Fig. 5), when omitting the penetrated Bi, the ratio of the elements Sb, Fe, Cr, and Ni is quite stable with ~ 48 at% Sb, ~ 39 at% Fe, ~ 9 at% Cr, and ~ 4 at% Ni. At all three locations shown in Fig. 5, region B is penetrated by Bi from the positive electrode side, though to different extents. The Bi penetration generally increases towards the edge of the cell and finally dominates the entire region B at the cell edge, see Figs. 5c and 6b.

Another common feature observed throughout the entire PCC surface is a chain of distinct Sb-rich precipitates (region C), see Figs. 5 and 6. They are separated from region B by a more or less thick layer of positive electrode alloy (mainly Bi). The composition of the Sb-rich precipitates of region C (~ 51 at% Sb, ~ 34 at% Fe, ~ 9 at% Cr, ~ 5 at% Ni) resembles the one of region B, though region C shows a slightly higher Sb content and a slightly lower Fe content. In contrast to region B, region C is not penetrated by Bi. Directly below the chain of Sb-rich precipitates, a small oxygen enrichment is observed (Figs. 5 and 6), indicating the remains of an earlier oxide layer at the original sample surface. In Fig. 6b, these remains are found along two lines, which are separated by penetrated Bi (positive electrode alloy).

The molar ratio of the elements Sb:(Fe + Cr + Ni) of about 1:1 in both region B and region C indicates formation of the non-stoichiometric compounds FeSb, CrSb, and NiSb, forming a solid solution (Fe,Cr,Ni)Sb. Based on the phase diagrams of the binary systems Fe-Sb, Cr-Sb, Ni-Sb and of the ternary systems Fe-Cr-Sb [23] and Fe-Ni-Sb [24], the measured compositions suggest additional formation of the solid solution (Fe,Cr)Sb₂, in particular in region C. Note the asymmetric composition of the compound FeSb with homogeneity range 43–45 at% Sb/(Sb + Fe).

Concerning the corrosion depth, the regions A, B, and C sum up to a total corrosion layer thickness of around 12–18 μm at the cell bottom and up to 40 μm at the cell edge (Fig. 6b). With 1500 h at operating temperature, an average corrosion rate of 0.008–0.012 $\mu\text{m}/\text{h}$ is deduced (0.027 $\mu\text{m}/\text{h}$ for the cell edge). This does not consider the Bi penetration shown in Figs. 5b and 6b, which leads to a separation of region C from the corroded steel (regions A and B).

The typical appearance of Mo after its service as PCC in a Na//SbBi₉ LMB cell operating for 1200 h is presented in Fig. 7. The line scan reveals diffusion of Mo into the positive electrode alloy (note the clear asymmetry of the Bi and Mo profiles at the surface of the Mo specimen).

4. Discussion

Molybdenum shows generally a very good corrosion resistance when exposed to (Na-)SbBi₉ alloys at temperatures around 450 °C, both in static (Figs. 3 and 4) and in cycling conditions (Fig. 7). In all cases, a minor diffusion of Mo into the adjacent alloy occurred. In none of the experiments, the corrosion process is affected by the presence of small amounts of oxygen. Cycling conditions have no measurable influence on the corrosion of Mo.

In contrast to Mo, the corrosion of stainless steels is crucially affected by the presence and action of oxygen, in particular regarding the static exposure to Na-Sb-Bi. No signs of an oxide layer could be found after static exposures to SbBi₉ (Fig. 4). Instead, the corrosion attack of 316L is

characterized by a 7–9 μm thick, compact corrosion layer of Fe-Cr-Sb compounds, namely the solid solution (Fe,Cr,Ni)Sb. With an exposure time of 740 h, an average corrosion rate of 0.009–0.012 $\mu\text{m}/\text{h}$ is deduced. Since similar corrosion layers were observed even for the ferritic steel T91 [22] after static exposure to SbBi₉, no significant differences regarding the composition of the corrosion layer or its thickness are expected for 316Ti either. Although the oxygen potential during the exposure was high enough for oxidation of Cr to Cr₂O₃ from a thermodynamic point of view, the kinetics of oxygen supply and/or of oxide formation is obviously not fast enough to form a continuous oxide layer that can mitigate the other corrosion processes such as the dissolution of steel alloying elements and the penetration of Sb.

The situation is different for static exposure to the ternary alloy Na_{0.30}Sb_{0.07}Bi_{0.63}. Here, all tested stainless steels (304, 316L, 316Ti) show a thin oxide layer on their surfaces (Fig. 2). In addition to the oxide layer, some dissolution of steel alloying elements and penetration of Bi and Sb into the steels is observed. However, the amount of penetrated Sb is not high enough to form a compact layer of Sb-compounds as corrosion products.

Inside the sealed exposure chambers, the initial oxygen content in the gas phase above the molten Na-Sb-Bi alloy (up to 1 ppm) is much larger than for the exposure experiments in the open crucibles containing SbBi₉ (below 10⁻³⁴ bar). Similarly, also the initial amount of oxygen dissolved in the ternary alloy, though limited by the oxidation potential of Na, is much larger than the amount of oxygen dissolved in SbBi₉. Since the free enthalpy of formation of Na₂O is close to the one of Cr₂O₃ and clearly above the one of ternary oxides such as CrNaO₂, formation of Cr-rich oxides at the sample surface are thermodynamically enabled. Indeed, a Cr-rich oxide (in some locations also enriched in Mo) is found on the sample surfaces after exposure to Na-Sb-Bi alloy (Fig. 2). Oxide scale formation continues until all available oxygen in the sealed reaction chambers is consumed and an equilibrium is reached.

The comparison of the static exposure tests in Na_{0.30}Sb_{0.07}Bi_{0.63} with the ones in SbBi₉ leads to the conclusion that the addition of Na to SbBi₉ strongly mitigates the corrosion of stainless steel thanks to the presence of oxygen. Na enables and facilitates the formation of ternary oxides on the sample surface, which mitigate diffusion and thus dissolution corrosion, penetration of Bi and Sb, and formation of Fe-Sb corrosion products (solid Sb-compounds).

The situation in a cycling cell is once again slightly different. As in the static exposure to Na-Sb-Bi, a rather large but limited amount of oxygen is present in the sealed LMB cell. During cycling, Na is alloyed with the positive electrode and enables formation of ternary oxides on the surface of the PCC. As time proceeds, however, stronger oxide formers present in the cell (in particular Li) catch the available oxygen, including the oxygen bound in oxides at the surface of the PCC. The described scenario regarding the distribution of oxygen in the test cell and its temporal evolution closely resembles the oxygen situation in real-scale liquid metal batteries. Small deviations might occur due to the differences in size. In particular, the transition from initially oxidizing conditions to the stage when the oxygen is bound by stronger oxide formers (Li) might be retarded in larger cells. After 1500 h exposure in the Na//SbBi₉ LMB test cell at operating temperature, thereof 1336 h under continuous cycling conditions, SS 316Ti shows a corrosion layer composed of different regions (Figs. 5 and 6). The steel is depleted in Cr and Ni at the corrosion front and penetration of Sb (strong) and Bi (mild) is observed (region A). Adjacent is a more compact layer composed of Fe-Cr-Ni-Sb compounds (region B), which is more or less penetrated by Bi from the positive electrode side. Finally, a layer of stable precipitates is found detached from the specimen surface (region C). Remains of a previously formed oxide layer are found directly below region C. They suggest that region C formed above the original sample surface. The solid solution (Fe,Cr,Ni)Sb, presumably with some additional (Fe,Cr)Sb₂, identified in the corrosion layer (regions B and C) of 316Ti after exposure to cycling conditions resembles the layer of solid solution (Fe,Cr,Ni)Sb found after static exposure to SbBi₉. As the layer of (Fe,Cr,Ni)

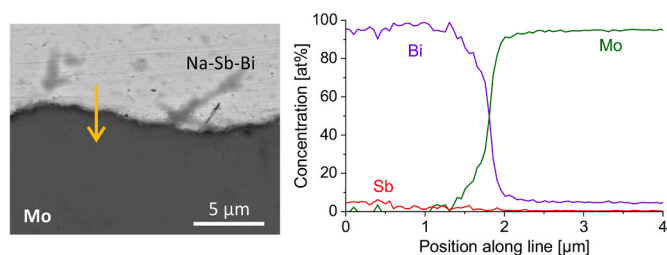


Fig. 7. SEM cross-section analysis of Mo after its service as PCC in a Na//SbBi₉ LMB cell operating for 1200 h.

Sb in static corrosion, also the layer of (Fe,Cr,Ni)Sb + (Fe,Cr)Sb₂ formed under cycling conditions is supposed to mitigate the corrosion attack by Bi. Precondition for corrosion mitigation, however, is the formation of a compact layer that does not easily detach from the sample surface. These conditions are fulfilled neither by region C (detached, Fig. 5b) nor by region B, in particular at the cell edge (not compact, Figs. 5c and 6b). As a consequence, dissolution attack and Bi penetration are enhanced and a significantly deeper attack is obtained at the cell edge (factor 2).

Regarding the average corrosion rate of SS 316Ti under cycling conditions, values between 0.008 and 0.012 $\mu\text{m}/\text{h}$ were deduced for the central part where a compact and adherent layer of Fe-Cr-Ni-Sb compounds is formed. This corrosion rate compares very well with the average static corrosion rate in SbBi₉ (0.009–0.012 $\mu\text{m}/\text{h}$). Additional effects not found in static corrosion and thus attributable to the cycling dynamics are the locally large penetration of Bi into the space between region B and region C, the detachment of region C, and the higher corrosion depths towards the cell edges.

Corrosion-enhancing processes in an LMB cell under cycling conditions could be the dynamically changing composition of the positive electrode, applied electric currents and potential differences across the interface, or liquid metal flow. Flow of the positive electrode alloy is typically driven by electromagnetic forces or density differences due to inhomogeneous temperature and concentration fields [25–29]. Convection is expected to increase the mass transport and homogenize the concentration of dissolved PCC species in the Na-Sb-Bi alloy. However, the anticipated velocities in the lab-scale LMB cells of this study are too low to cause erosion-corrosion. Regarding electric currents and the dynamically changing composition of the positive electrode, Fig. 8 presents simulation results that demonstrate the inhomogeneity of these effects during cell operation. The current density in the positive electrode has its maximum values at the upper edges (three-phase contact line between positive electrode, molten salt, and PCC) and its smallest values at the lower edges (cell edge). Thus, the enhanced corrosion depth at/next to the cell edge cannot be explained by an enhanced electric current or potential drop across the interface at this location. The inhomogeneous current density distribution in the molten salt, on the other hand, results in a higher Na-alloying/dealloying activity of the positive electrode in the cell center, which might well cause different corrosion conditions at the surface of the PCC in the cell center and at the cell edge.

Despite the deviating conditions in a cycling cell, the static corrosion tests in SbBi₉ give a good indication of the corrosion behavior in an operating Na/SbBi₉-LMB cell with Na concentrations up to 22 mol% in the positive electrode.

5. Conclusion

Static material compatibility tests of stainless steel and molybdenum in liquid Sb-Bi and Na-Sb-Bi alloys at 450 °C showed that the presence of 30 mol% Na in the liquid metal alloy mitigates the corrosion attack. For stainless steel, which exhibits a 7–9 μm thick corrosion layer composed of Fe-Cr-Ni-Sb compounds after 740 h exposure to SbBi₉, a corrosion depth below 1 μm is observed after 750 h exposure to Na_{0.30}Sb_{0.07}Bi_{0.63}. Reason for the better corrosion resistance is the formation of an oxide layer due to the higher oxygen activity and the presence of Na in the ternary alloy. Cycling conditions with a Na content between 5 and 22 mol% in the positive electrode, however, lead to corrosion rates similar to the ones of static exposure to Na-free SbBi₉. After its use as PCC material in an operating Na/LiCl-NaCl-KCl/SbBi₉ liquid metal battery, stainless steel 316Ti exhibits a corrosion layer composed of different regions showing Sb penetration, Bi penetration, and formation of Fe-Cr-Ni-Sb compounds. Additionally, some remains of a previously formed oxide layer are found. The presence of stronger oxide formers (Li) in the cell prevents the formation of a stable, corrosion-mitigating oxide layer on the surface of the PCC. Dissolution of steel alloying elements, penetration of liquid metal, and formation of solid corrosion products result.

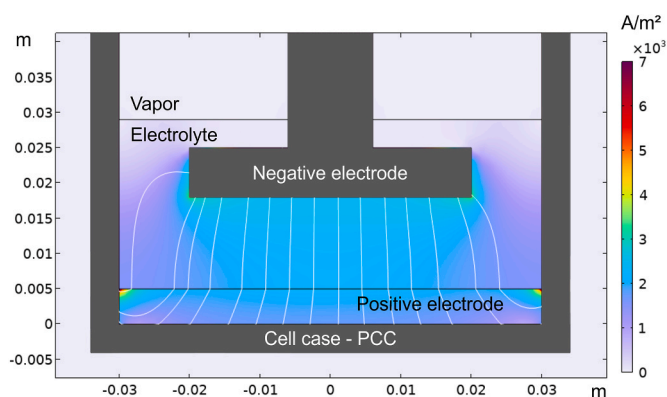


Fig. 8. Simulation results of current density in cell when charged/discharged with a current of 5 A. Weight solid lines show a few exemplary streamlines.

Compared with static corrosion, dynamic cycling conditions cause additional corrosion features and an accelerated corrosion process. Further experiments (e.g., systematic variation of the current density) are required to pinpoint the cause of the enhanced corrosion in cycling conditions.

Corrosion enhancement in cycling conditions is not observed for Mo. Although Mo does not show the formation of an oxide layer in any of the experiments, it exhibits a very good corrosion resistance when exposed to Sb-Bi or Na-Sb-Bi alloys. A minor dissolution/diffusion of Mo into the adjacent liquid metal alloy is found both in static and in cycling conditions.

The good performance of Mo as positive current collector material still needs to be confirmed in long-term cycling tests, since the study presented here concerns tests of two months duration only, which is much shorter than the envisaged service life of LMB cells.

Data availability

The raw/processed data required to reproduce these findings cannot be shared at this time due to technical or time limitations. The data are available from the corresponding author on reasonable request.

CRediT authorship contribution statement

Renate Fetzer: Writing – original draft, Investigation, Conceptualization. **Tianru Zhang:** Investigation. **Annette Heinzl:** Writing – review & editing, Investigation. **Alfons Weisenburger:** Writing – review & editing, Conceptualization. **Georg Müller:** Project administration, Funding acquisition.

Declaration of competing interest

The authors declare that they have no known competing financial interests or personal relationships that could have appeared to influence the work reported in this paper.

Acknowledgments

The authors are grateful to the Deutsche Forschungsgemeinschaft (DFG) and National Natural Science Foundation of China (NSFC) for funding the DFG-NSFC Sino-German Project (DFG Project Member 411450529): “Study on Corrosion Control and Low-Temperature Electrolytes for Low-Cost Na-based Liquid Metal Batteries”.

References

- [1] H. Kim, D.A. Boysen, J.M. Newhouse, B.L. Spatocco, B. Chung, P.J. Burke, D. J. Bradwell, K. Jiang, A.A. Tomaszowska, K. Wang, W. Wei, L.A. Ortiz, S.A. Barriga,

- S.M. Poizeau, D.R. Sadoway, Liquid metal batteries: past, present, and future, *Chem Rev* 113 (2013) 2075–2099, <https://doi.org/10.1021/cr300205k>.
- [2] Y. Ding, X. Guo, G. Yu, Next-generation liquid metal batteries based on the chemistry of fusible alloys, *ACS Cent. Sci.* 6 (2020) 1355–1366, <https://doi.org/10.1021/acscentsci.0c00749>.
- [3] S. Wu, X. Zhang, R. Wang, T. Li, Progress and perspectives of liquid metal batteries, *Energy Storage Mater.* 57 (2023) 205–227, <https://doi.org/10.1016/j.ensm.2023.02.021>.
- [4] Q. Zeng, Z. Lv, S. Li, B. Yang, J. He, J. Song, Electrolytes for liquid metal batteries, *Mater. Res. Bull.* 170 (2024) 112586, <https://doi.org/10.1016/j.materresbull.2023.112586>.
- [5] D.H. Kerridge, The solubility of metals in liquid metals, *J. Nucl. Energy Part B - React. Technol.* 1 (1961) 215–220, [https://doi.org/10.1016/S0368-3273\(15\)30031-6](https://doi.org/10.1016/S0368-3273(15)30031-6).
- [6] *Handbook on Lead-bismuth Eutectic Alloy and Lead Properties, Materials Compatibility, Thermal-hydraulics and Technologies*, OECD Publishing, Paris, 2015.
- [7] A. Heinzl, A. Weisenburger, G. Müller, Corrosion behavior of austenitic steel AISI 316L in liquid tin in the temperature range between 280 and 700 °C, *Mater. Corros.* 68 (2017) 831–837, <https://doi.org/10.1002/maco.201609211>.
- [8] K. Wang, K. Jiang, B. Chung, T. Ouchi, P.J. Burke, D.A. Boysen, D.J. Bradwell, H. Kim, U. Muecke, D.R. Sadoway, Lithium-antimony-lead liquid metal battery for grid-level energy storage, *Nature* 514 (2014) 348–350, <https://doi.org/10.1038/nature13700>.
- [9] S. Yan, X. Zhou, H. Li, Y. Shen, Y. He, H. Zhou, K. Wang, K. Jiang, Utilizing in situ alloying reaction to achieve the self-healing, high energy density and cost-effective Li||Sb liquid metal battery, *J. Power Sources* 514 (2021) 230578, <https://doi.org/10.1016/j.jpowsour.2021.230578>.
- [10] H. Li, K. Wang, S. Cheng, K. Jiang, High performance liquid metal battery with environmentally friendly antimony-tin positive electrode, *ACS Appl. Mater. Interfaces* 8 (2016) 12830–12835, <https://doi.org/10.1021/acsami.6b02576>.
- [11] K. Cui, P. Li, W. Zhao, S. Li, C. Liu, X. Qu, Electrochemical performance and application prospect analysis of Li||Sb-Bi-Sn liquid metal batteries, *Mater. Lett.* 338 (2023) 134067, <https://doi.org/10.1016/j.matlet.2023.134067>.
- [12] T. Ouchi, D.R. Sadoway, Positive current collector for Li||Sb-Pb liquid metal battery, *J. Power Sources* 357 (2017) 158–163, <https://doi.org/10.1016/j.jpowsour.2017.04.104>.
- [13] K. Cui, F. An, W. Zhao, P. Li, S. Li, C. Liu, X. Qu, Feasibility research of SS304 serving as the positive current collector of Li||Sb-Sn liquid metal batteries, *J. Phys. Chem. C* 125 (2021) 237–245, <https://doi.org/10.1021/acs.jpcc.0c09629>.
- [14] K. Cui, P. Li, W. Zhao, C. Liu, S. Li, D. Zhou, X. Qu, Self-healing action of Bi in high-performance Sb-Bi-Sn positive electrodes for liquid metal batteries, *J. Power Sources* 538 (2022) 231584, <https://doi.org/10.1016/j.jpowsour.2022.231584>.
- [15] K. Cui, W. Zhao, D. Zhou, S. Li, C. Liu, P. Li, X. Qu, Stable positive current collectors for Li||Sb-Sn liquid metal batteries, *ACS Appl. Energy Mater.* 4 (2021) 9013–9021, <https://doi.org/10.1021/acsaem.3c01280>.
- [16] W. Ding, Q. Gong, S. Liang, R. Hoffmann, H. Zhou, H. Li, K. Wang, T. Zhang, A. Weisenburger, G. Müller, A. Bonk, Multi-cationic molten salt electrolyte of high-performance sodium liquid metal battery for grid storage, *J. Power Sources* 553 (2023) 232254, <https://doi.org/10.1016/j.jpowsour.2022.232254>.
- [17] H. Zhou, H. Li, Q. Gong, S. Yan, X. Zhou, S. Liang, W. Ding, Y. He, K. Jiang, K. Wang, A sodium liquid metal battery based on the multi-cationic electrolyte for grid energy storage, *Energy Storage Mater.* 50 (2022) 572–579, <https://doi.org/10.1016/j.ensm.2022.05.032>.
- [18] R. Fetzter, T. Zhang, F. Lindner, A. Weisenburger, G. Müller, How cell design affects the performance of sodium-antimony-bismuth liquid metal batteries, *J. Power Sources* 591 (2024) 233823, <https://doi.org/10.1016/j.jpowsour.2023.233823>.
- [19] T. Zhang, A. Heinzl, A. Jianu, A. Weisenburger, G. Müller, Corrosion investigations of materials in antimony-tin and antimony-bismuth alloys for liquid metal batteries, in: *TMS 2021 150th Annual Meeting & Exhibition Supplemental Proceedings*, Springer International Publishing, Cham, 2021, pp. 605–614.
- [20] T. Zhang, R. Fetzter, A. Heinzl, A. Weisenburger, C. Tang, M. Stüber, G. Müller, Corrosion behavior of various conductive materials in Sb3Sn7 alloy at 450 °C, *Corros Sci* 227 (2024) 111797, <https://doi.org/10.1016/j.corsci.2023.111797>.
- [21] W. Liu, H. Yin, K. Du, B. Yang, D. Wang, Corrosion behaviors of iron, chromium, nickel, low-carbon steel, and four types of stainless steels in liquid antimony-tin alloy, *Corrosion* 77 (2021) 1192–1202, <https://doi.org/10.5006/3820>.
- [22] R. Fetzter, A. Heinzl, T. Zhang, A. Weisenburger, G. Müller, Corrosion of austenitic and ferritic steels, Kovar, and molybdenum in liquid Sb-Bi alloys with different compositions, *Corros Sci* 233 (2024) 112115, <https://doi.org/10.1016/j.corsci.2024.112115>.
- [23] Y. Xia, Y. Liu, C. Wu, H. Peng, H. Tu, J. Wang, X. Su, 650 and 750 °C isothermal sections of the Cr-Sb-Fe system, *J. Phase Equilibria Diffus.* 39 (2018) 426–436, <https://doi.org/10.1007/s11669-018-0653-0>.
- [24] V. Rahavan, Fe-Ni-Sb (iron-nickel-antimony), *J. Phase Equilibria Diffus.* 25 (2004) 89–91, <https://doi.org/10.1007/s11669-004-0181-y>.
- [25] R.F. Ashour, D.H. Kelley, Convection-diffusion model of lithium-bismuth liquid metal batteries, in: *Minerals, Metals and Materials Series*, 2018, pp. 41–52, https://doi.org/10.1007/978-3-319-72131-6_4.
- [26] D.H. Kelley, T. Weier, Fluid mechanics of liquid metal batteries, *Appl. Mech. Rev.* 70 (2018), <https://doi.org/10.1115/1.4038699>.
- [27] N. Weber, M. Nimitz, P. Personnetaz, A. Salas, T. Weier, Electromagnetically driven convection suitable for mass transfer enhancement in liquid metal batteries, *Appl. Therm. Eng.* 143 (2018) 293–301, <https://doi.org/10.1016/j.applthermaleng.2018.07.067>.
- [28] P. Personnetaz, S. Landgraf, M. Nimitz, N. Weber, T. Weier, Mass transport induced asymmetry in charge/discharge behavior of liquid metal batteries, *Electrochem. Commun.* 105 (2019), <https://doi.org/10.1016/j.elecom.2019.106496>.
- [29] X. Zhou, C. Gao, Y. Shen, H. Li, S. Yan, H. Zhou, K. Wang, K. Jiang, Multi-field coupled model for liquid metal battery: comparative analysis of various flow mechanisms and their effects on mass transfer and electrochemical performance, *Energy Rep.* 8 (2022) 5510–5521, <https://doi.org/10.1016/j.egyrr.2022.04.018>.